Self-assembly nanomicelle-microneedle patches with enhanced tumor penetration for superior chemo-photothermal therapy

Ying Sun[1,§], Minglong Chen[1,4,§], Dan Yang[2], Wanbing Qin[3], Guilan Quan[2] (✉), Chuanbin Wu[2], and Xin Pan[1] (✉)

[1] School of Pharmaceutical Sciences, Sun Yat-sen University, Guangzhou 510006, China
[2] College of Pharmacy, Jinan University, Guangzhou 510632, China
[3] Jieyang Affiliated Hospital, Sun Yat-Sen University, Guangzhou 522091, China
[4] Physical Sciences at the Microscale, Department of Polymer Science and Engineering, University of Science and Technology of China, Hefei 230026, China
[§] Ying Sun and Minglong Chen contributed equally to this work.

ABSTRACT

Nanomedicine with high specificity has been a promising tool for cancer diagnosis and therapy. However, the successful application of nanoparticle-based superficial cancer therapy is severely hindered by restricted deep tumor tissue accumulation and penetration. Herein, a self-assembly nanomicelle dissolving microneedle (DMN) patch according to the "nano in micro" strategy was conducted to co-deliver a first-line chemotherapeutic agent paclitaxel (PTX), and a photosensitizer IR780 (PTX/IR780-NMs @DMNs) for chemo-photothermal synergetic melanoma therapy. Upon direct insertion into the tumor site, DMNs created a regular and multipoint three-dimensional drug depot to maximize the tumor accumulation. Accompanied by the DMN dissolution, the composition of the needle matrixes self-assembled into nanomicelles, which could efficiently penetrate deep tumor tissue. Upon laser irradiation, the nanomicelles could not only ablate tumor cells directly by photothermal conversion but also trigger PTX release to induce tumor cell apoptosis. *In vivo* results showed that compared with intravenous injection, IR780 delivered by PTX/IR780-NMs @DMNs was almost completely accumulated at the tumor site. The antitumor results revealed that the PTX/IR780-NMs @DMNs could effectively eliminate tumors with an 88% curable rate without any damage to normal tissues. This work provides a versatile and generalizable framework for designing self-assembly DMN-mediated combination therapy to fight against superficial cancer.

KEYWORDS

dissolving microneedle, tumor penetration, nanomicelle, superficial tumor, chemo-photothermal therapy

1   Introduction

Nanomedicine-based cancer therapy has gained extensive attention in recent years. Typical nanostructures, such as liposome, metal-organic framework, mesoporous silicon, and polymeric nanomicelle are widely employed to encapsulate therapeutic drugs with enhanced bioavailability and stability [1]. The versatile nanocarriers can provide diverse options for multimodal synergistic therapy to achieve "two birds with one stone" or "all in one" antitumor strategies [2]. Intravenous injection (I.V.) is the main administration method for these nanoscale delivery systems. However, the systemic circulation severely impedes efficient drug accumulation at the tumor sites, leading to insufficient drug dosage and unsatisfied antitumor efficiency. Besides, the deep tumor penetration of nanoparticles is limited by the specific pathophysiological microenvironment of solid tumors, which results from the heterogeneous vasculature, high interstitial fluid pressure, and dense stroma [3]. Recent studies reveal that nanoparticles' intratumoral transport mostly depends on the diffusion mobility within the tumor interstitium which is closely associated with their particle size [4]. Researches show that nanoparticles with smaller hydrodynamic size can facilitate better penetration in solid tumors [5, 6]. Paradoxically, small-sized nanoparticles are more likely to leak out from the tumor interstitium, causing unpredictable systemic distribution [7]. The unwished drug distribution at the normal tissues greatly harms the physiological functions, resulting in a series of side effects. These drawbacks caused by systemic administration restrict the application of nanomedicine, especially for superficial cancer therapy.

Transdermal drug delivery (TDD) systems have shown great promise for superficial tumor treatment by increasing tumor accumulation of cargos and reducing systemic toxic effects [8]. However, the stratum corneum as the natural barrier severely hinders the efficient TDD of nanoparticles and biomacromolecules. Dissolving microneedle (DMN) system has been developed as an attractive TDD platform to improve drug delivery efficiency across the skin [9]. A microneedle patch comprises hundreds of micron-scaled needles arranged on a supporting base, which can form regular-arranged microchannels across the stratum corneum in a minimally invasive manner. DMNs can directly target the lesion site and form a multipoint drug depot *in situ* to facilitate drug accumulation and uniform

distribution at the tumors [10–12]. In addition, the materials used for DMN fabrication, including carbohydrates (e.g., maltose, chitosan, dextran, cellulose, and hyaluronic acid (HA)), proteins (e.g., gelatin, silk fibroin, and albumin), and aliphatic polymers (e.g., polyvinyl alcohol (PVA) and polyvinyl pyrrolidone (PVP)), are water-soluble, biodegradable, and biocompatible [9]. Thus, the fabricated DMNs can completely dissolve in the dermal interstitial fluid without any residue after insertion into the skin, thereby releasing the encapsulated cargos along with the DMNs dissolution. But these water-soluble DMNs only enable to encapsulate hydrophilic drugs, and the drug loading amount is limited, which curbs their further application in hydrophobic drug delivery [9, 13, 14]. Surprisingly, using the "nano in micro" strategy to integrate the merits of the nanotechnology and the DMN system (Nano-DMN) can not only improve the drug loading of hydrophobic drugs but also overcome the obstacles of nanoparticle transdermal delivery. Encouraged by the advantages aforementioned, Nano-DMN systems have been widely explored for vaccination [11, 15, 16], blood glucose regulation [17–19], and superficial skin cancer treatment [20–22].

Malignant melanoma is one of the most aggressive skin cancers that makes up 4% of skin cancer incidence but accounts for most mortalities [20, 21]. Traditional excisional surgery for melanoma at an early stage is quite invasive with the risk of inflammation, which is unbearable for some patients with other diseases such as heart failure [21]. Additional treatments, including immunotherapy or radiotherapy, are often recommended after surgery if tumor tissues are incompletely removed. However, the significant side effects of immune response and radiation resistance restrict their widespread application [20]. Chemotherapy is a classic antitumor strategy, which has unsatisfied efficacy in malignant melanoma ascribed to the short response duration, common drug resistance, and severe systemic toxicity. Recently, photothermal therapy (PTT) has been considered as a promising approach to improve survival. PTT can convert external near-infrared (NIR) light energy into hyperthermia to induce thermal ablation by using photothermal agents, resulting in irreversible damage to tumor cells [23]. The local hyperthermia can also improve the cell membrane permeation to promote nanoparticle internalization and trigger drug release, therefore enhancing chemotherapy sensitivity. Moreover, PTT is a minimally invasive local treatment strategy that can be precisely controlled with reduced systemic toxicity [24–26]. Our previous study has proved that the combination of chemotherapy and PTT could achieve synergistically enhanced antitumor efficacy [27].

Herein, based on the "nano in micro" strategy, we fabricated a paclitaxel (PTX) and IR780-loaded nanomicelle microneedle system (PTX/IR780-NMs @DMNs) for transdermal melanoma therapy with enhanced tumor accumulation and deep tumor permeation (Fig. 1). PTX is a standard first-line chemotherapy drug widely used to treat solid tumors [28]. Photosensitizer IR780 is a derivative of indocyanine green that has been approved by FDA. Compared to indocyanine green, IR780 has stronger photostability and higher photothermal conversion efficacy [29]. However, the hydrophobic property of PTX and IR780 aggravates the difficulty in practical application [30, 31]. In this work, commercial available amphiphilic polymer Soluplus® is employed to improve the drug solubility, which can self-assemble into micelles in an aqueous environment even at a low concentration (critical micelle concentration: 7.6 mg/L in water at 23 °C), simultaneously accompanied with efficient encapsulation of the water-insoluble drugs (e.g., PTX and IR780) into the hydrophobic core [32, 33]. Additionally, HA, an endogenous component of the human body, is used as the matrix material of the DMNs, since it is non-immunogenic, biodegradable, and dissoluble. For administration, the PTX/IR780-NMs @DMN patch was precisely applied at the tumor site, successfully pierced through the stratum corneum, and formed a local multipoint drug depot to achieve tumor accumulation. Subsequently accompanied by the DMNs dissolution, the *in situ* self-assembly PTX/IR780-NMs could diffuse into the deep tumor tissues due to their small particle size. Under NIR light irradiation, IR780 could cause local hyperthermia and generate robust reactive oxygen species (ROS), cooperating with chemotherapy to kill the tumor cells. The *in vivo* experiments showed that PTX/IR780-NMs @DMNs had better tumor inhibition efficacy than PTX or IR780 treatment alone. This work confirmed that the self-assembly Nano-DMN system exhibited
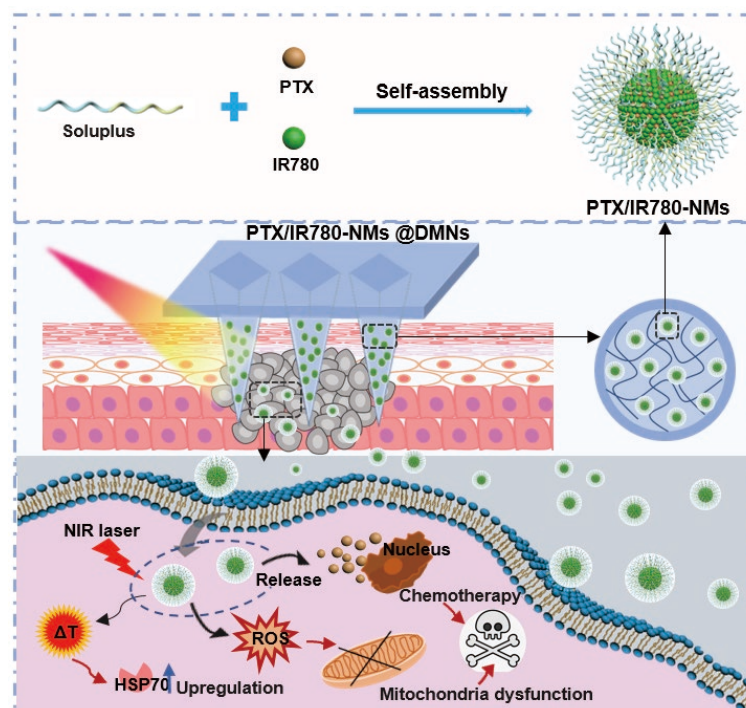

Figure 1 Schematic illustration of self-assembly nanomicelle microneedle patches for chemo-photothermal therapy.

great potential in the combination therapy against superficial tumors.

2 Methods

2.1 Preparation and characterization of PTX/IR780 NMs

PTX/IR780-NMs were prepared by the thin-film dispersion method. Briefly, PTX, IR780, and Soluplus® with the weight ratio of 1:1:50 were mixed and dissolved in ethanol and stirred at room temperature until forming a homogeneous solution. Then, the organic solvent was evaporated completely in a vacuum at 40 °C for 1.5 h. Subsequently, 1 mL of ultrapure water was added and stirred at 500 rpm for 30 min to hydrate the drug-loaded thin film to obtain micelle solution. PTX-NMs, IR780-NMs, and blank-NMs were also fabricated by the similar procedure mentioned above.

The particle size, polydispersity index (PDI), and zeta potential of various nanomicelles were analyzed using the dynamic light scattering (Zetasizer Nano, Malvern Instrument, UK). The morphology of PTX/IR780-NMs was characterized by transmission electron microscopy (TEM, JEM1400, Hitachi, Japan). The stability of PTX/IR780-NMs was investigated by measuring the particle size change during the storage at 4 °C for 10 days. The emission wavelength of free IR780 and PTX/IR780-NMs in ethanol solution under an excitation wavelength of 763 nm was detected using a fluorescence spectrometer (Floromax-4, USA). The encapsulation efficiency (EE) of PTX was determined by high-performance liquid chromatography (HPLC, LC-20AT, Shimadzu, Japan). And the EE of IR780 was measured by a fluorescence spectrometer. The EE was calculated using the following formula:

EE% = (W_i / W_{total})×100%, where W_i is the amount of encapsulated PTX or IR780 in the NMs, W_{total} is the total amount of PTX or IR780.

2.2 Photothermal property of PTX/IR780-NMs

To explore the photothermal property of PTX/IR780-NMs, the micelle solution (1.094, 2.188, 4.375, 8.750 µg/mL of IR780) was irradiated under 808 nm NIR laser at a power density of 1 W/cm² for 5 min. The temperature was monitored every 30 s using a visual infrared thermal imaging camera (Tis75, Fluke, USA).

2.3 *In vitro* cytotoxicity

Cells were cultured in RPMI 1640 medium supplemented with 10% FBS and 1% penicillin-streptomycin and incubated at 37 °C in a 5% CO_2 humidified atmosphere.

2.3.1 Cell viability

Cell viability was determined by the CCK-8 assay. Briefly, B16 cells were seeded in a 96-well plate at a density of 8×10^3 per well and cultured for 24 h, followed by exposure to PTX/IR780-NMs, PTX-NMs, IR780-NMs, and blank NMs with different concentrations for 2 h. Next, the cells co-incubated with PTX/IR780-NMs and IR780-NMs were irradiated with NIR laser at 808 nm (1 W/cm²) for 3 min. After incubation for another 24 h, the previous medium containing NMs was replaced with fresh RPMI-1640 medium, and CCK-8 kit was added to each well for an additional 1 h of incubation. The cell viability was calculated by measuring the absorption at 450 nm using a microplate reader (ELx800, Biotek, USA).

2.3.2 Calcein-AM/PI staining

B16 cells were seeded into a 24-well plate at a density of 8×10^4 cells per well and allowed to adhere overnight. Cells were then exposed to PTX/IR780-NMs, PTX-NMs, IR780-NMs, and blank-NMs with a concentration of 10 µg/mL PTX and 5 µg/mL IR780 for 2 h. The samples containing IR780 were irradiated with a laser (808 nm, 1 W/cm²) for 3 min, followed by incubation for another 12 h. After removal of the nanomicelle-containing medium, the cells were stained with Calcein-AM/PI kit (BestBio, Shanghai, China) according to the manufacturer's instruction and further visualized by a cell imaging system (EVOS FL Auto, USA). Calcein AM $\lambda_{ex/em}$: 490/515 nm, PI $\lambda_{ex/em}$: 535/617 nm.

2.4 Cellular uptake and organelle colocalization

Coumarin-6 (C6) was used to replace PTX and co-loaded with IR780 into the nanomicelles (C6/IR780-NMs). For *in vitro* cellular uptake, the fresh medium containing C6/IR780-NMs was added after removal of culture medium. After incubation for 0.5 h (or 2 h), the cells were washed twice with PBS, followed by fixing with 4% paraformaldehyde for 10 min. Then the cell nuclei were stained with DAPI and washed with PBS three times. Finally, the cells were observed using a confocal laser scanning microscope (CLSM, FV3000, Olympus, Japan). Coumarin-6 $\lambda_{ex/em}$: 466/504 nm, DAPI $\lambda_{ex/em}$: 358/461 nm.

To investigate the cellular organelle colocalization, the fresh medium containing C6-NMs was added after removal of the culture medium. After incubation for 2 h, the cells were washed with PBS three times. The mitochondria and lysosome were stained with MitoTracker® Red CMXRos (M9940, Solarbio, Beijing, China) and BBcellProbeTM L03 (BB-44121, BestBio, Shanghai, China) respectively for 45 min under 5% CO_2 at 37 °C. Then the cell nuclei were stained with DAPI and washed with PBS three times. Finally, the cells were analyzed by CLSM. MitoTracker® Red CMXRos $\lambda_{ex/em}$: 579/599 nm, BBcellProbeTM L03 $\lambda_{ex/em}$: 577/590 nm.

2.5 Microtubulin immunofluorescence analysis in B16 cells

B16 cells were seeded into a glass-bottom dish at a density of 2×10^5 per dish and allowed to adhere overnight. After removal of previous medium, fresh medium containing PTX/IR780-NMs, PTX-NMs, IR780-NMs, and blank-NMs were added. After incubation for 2 h, the cells treated with PTX/IR780-NMs and IR780-NMs were exposed to 808 nm laser (1 W/cm²) irradiation for 3 min, followed by incubation for another 2 h. Then the cells were washed by PBS three times and fixed with immunostaining fixative for 15 min at room temperature. Next, the cells were immune-stained by Tubulin-Tracker Red with cell nuclei stained by DAPI. Finally, the cells were imaged by CLSM. Tubulin-Tracker Red $\lambda_{ex/em}$: 555/565 nm.

2.6 Heat shock proteins (HSP 70) immunofluorescence staining

B16 cells were cultured in a 24-well glass-bottom plate at a density of 8×10^4 per well and cultured overnight. After incubation with various samples for 2 h, the B16 cells in PTX/IR780-NMs group and IR780-NMs group were exposed to laser irradiation (808 nm, 1 W/cm²) for 3 min. After being fixed with 4% paraformaldehyde, the cells were treated with immunofluorescence staining to investigate the expression of HSP 70.

2.7 ROS generation in B16 cells

B16 cells were seeded in a 24-well glass-bottom plate at a density of 8×10^4 per well and cultured overnight. The medium was replaced by a fresh medium containing PTX/IR780-NMs, PTX-NMs, IR780-NMs, and blank-NMs, respectively. DCFH-DA probe (10 µM) was used to detect the ROS. And cell nuclei were

stained with Hoechst 33342. The treated cells were observed by the CLSM. DCF $\lambda_{ex/em}$: 480/525 nm, Hoechst 33342 $\lambda_{ex/em}$: 350/461 nm.

2.8　JC-1 staining

B16 cells were seeded in a 24-well glass-bottom plate at a density of 8×10^4 cells/well and allowed overnight for cell adherence. Cells were co-cultured with different nanomicelles for 2 h and then treated with 808 nm NIR light irradiation (1 W/cm²) for 3 min. Finally, cells were stained with JC-1 dye to detect the mitochondrial membrane potential. JC-1 monomer $\lambda_{ex/em}$: 514/529 nm, JC-1 aggregates $\lambda_{ex/em}$: 585/590 nm.

2.9　Fabrication and characterization of PTX/IR780-NMs @DMNs

The DMNs were prepared by a three-step centrifugation method using a PDMS female mold containing needle cavities inversely replicated from a brass male structure. These needle cavities were arranged in a 12×12 array with 750 μm tip-to-tip spacing on a 9 mm × 9 mm patch, and each needle cavity was in a pyramid shape with 300 μm in base diameter and 800 μm in height.

The PTX/IR780-NMs @DMNs patches were prepared according to the procedure reported previously [21]. PTX/IR780-NMs suspension was cast into the female mold followed by centrifugation and drying to concentrate the nanomicelles into the needle tips. To increase the drug loading, PTX/IR780 NMs suspension was added and centrifuged twice. Subsequently, the HA solution (40 wt.% in water) was added to fill the needle cavities, and PVP K90 solution (30 wt.% in ethanol) was poured onto the mold to form the base. The DMNs were gently peeled off from the mold after drying completely. The PTX-NMs @DMNs, IR780 NMs-@DMNs, and blank-NMs @DMNs were also obtained using the same procedure.

To measure the amount of PTX and IR780 loaded in the DMNs, all needles were separated from the patch and then dissolved in ethanol. The amount of PTX and IR780 was determined by HPLC and fluorescence spectrometer, respectively.

To verify the self-assembly property, the needles of PTX/IR780-NMs @DMNs were separated from the patch and re-dissolved in ultrapure water or PBS. The particle size and morphology of the reconstituted MNs were measured by dynamic light scattering and TEM, respectively.

The morphology and dimension of the fluorescent DMNs were observed by microscope (Nikon, Tokyo, Japan) and scanning electron microscope (SEM). The drug distribution in fluorescent DMNs was visualized by CLSM.

2.10　*In vitro* skin insertion of PTX/IR780-NMs @DMNs

To test the skin insertion ability, trypan blue @DMNs were prepared. Briefly, trypan blue @DMNs were inserted into the hair-removed excised rat skin. The inserted skin surface was imaged by a camera after the removal of the DMNs.

To evaluate the drug diffusion in the skin, the fluorescent DMNs were pressed into the hair-removed excised rat skin. The skin sample was scanned by CLSM at 0.5, 1, 3, 5, 10 min after insertion of DMNs. To further investigate the drug penetration of PTX/IR780-NMs @DMNs to the deep tissue, fluorescent DMNs treated porcine skin was collected to prepare the frozen fluorescent section. The cross-section of DMNs treated skin was observed and imaged by CLSM.

2.11　*In vivo* photothermal property of PTX/IR780-NMs @DMNs

C57 female mice were anaesthetized, and the dorsal hair was

carefully shaved, followed by the application of depilatory cream. The PTX/IR780-NMs @DMNs were applied on the hair-removed dorsal skin. After removal of DMNs, the skin was irradiated under a laser (808 nm, 1 W/cm²) for 5 min. An infrared thermal imaging camera was used to record the temperature.

2.12　*In vivo* imaging and biodistribution

The melanoma animal model was built by subcutaneous injection of B16 cells at the back of C57 mice. The mice were randomly divided into 2 groups ($n = 3$): (1) PTX/IR780-NMs @DMNs, and (2) PTX/IR780-NMs @I.V. The real-time fluorescence signal was monitored using a live fluorescence imaging system (IVIS Lumina XRMS, PerkinElmer, USA) at various time points (0, 2, 4, 6, 12, 24, 48 h). After 48 h, all the mice were sacrificed, and major organs were excised to investigate the fluorescence signal distribution.

2.13　*In vivo* antitumor efficacy and safety

All animal experiments were performed following the protocol approved by the Institutional Animal Care and Use Committee of Sun Yat-sen University. C57 mice were subcutaneously injected with 1×10^6 B16 melanoma cells in the back to establish the animal model. When the tumor volume reached approximately 40–60 cm³, all tumor-bearing mice were randomly divided into 5 groups ($n = 6$): (1) no treatment, (2) PTX-NMs @DMNs, (3) PTX/IR780-NMs @DMNs, (4) IR780-NMs @DMNs +Laser, (5) PTX/IR780-NMs @DMNs +Laser. The DMNs were inserted into the tumor site with a thumb for 2 min and fixed in situ for 30 min. "+Laser" means laser (808 nm, 1 W/cm²) irradiation for 5 min at the tumor site immediately after removal of DMN patches. The tumor volume was measured every other day by a digital caliper and calculated by the formula: tumor volume = (long diameter × short diameter²)/2.

On the 10th day after administration, the mice were sacrificed, and the tumors were carefully extracted to measure the tumor weight. The tumors were then fixed with 4% formaldehyde, embedded in a paraffin block, sectioned into slices, and ultimately stained with H&E to further investigate the antitumor effect.

To assess the biosafety of DMNs, the mice were weighed every two days. The skin recovery after DMN treatment was conducted on the B16 melanoma-bearing mice with laser irradiation. The blood samples were collected and further used to evaluate the hepatorenal function. The major organs were also harvested and stained with H&E for histopathology analysis.

2.14　Statistical analysis

All data are expressed as mean ± standard deviation (SD). The statistical difference was determined by one-way ANOVA after normality test and variance homogeneity using SPSS 22.0 (SPSS Inc. Chicago, IL), and P-value < 0.05 was considered statistically significant. P values are indicated as follows: $^*P < 0.05$; $^{**}P < 0.01$; $^{***}P < 0.001$; $^{****}P < 0.0001$.

3　Results and discussion

3.1　Characterization of PTX/IR780-NMs

The PTX/IR780-NMs were prepared according to a thin-film dispersion method previously reported [34]. The average diameter of PTX/IR780-NMs was about 57.50 ± 0.63 nm with a narrow PDI of 0.15 ± 0.01 (Fig. 2(a)). The TEM image further confirmed the homogeneous particle size and spherical structure of PTX/IR780-NMs (Fig. 2(b)). The zeta potential of blank NMs, PTX-NMs, IR780-NMs, and PTX/IR780-NMs were –1.77, –2.35, +22.00, and +6.73 mV, respectively (Fig. 2(d)). The change in the
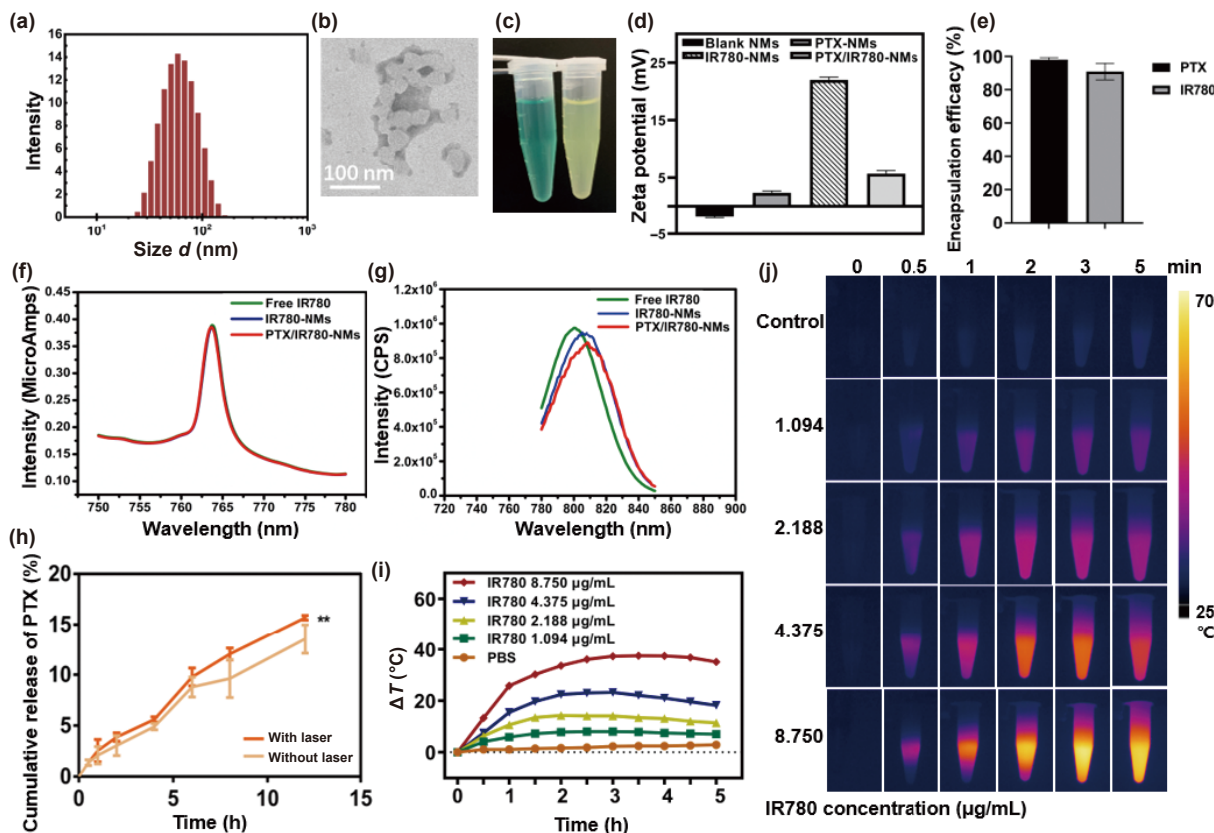
Figure 2 Characterization of PTX/IR780-NMs. (a) Particle size and (b) TEM image of PTX/IR780-NMs. (c) Photographs of PTX/IR780-NMs solution before and after NIR irradiation. (d) Zeta potential of various nanomicelles. (e) Drug encapsulation efficiency of PTX/IR780-NMs. (f) Fluorescence excitation spectra and (g) emission spectra of free IR780, IR780-NMs and PTX/IR780-NMs. (h) PTX release profiles from PTX/IR780-NMs after laser irradiation. (i) Temperature-time profiles and (j) photographs of PTX/IR780-NMs with different IR780 concentrations under NIR irradiation for 5 min. Data are expressed as the mean ± SD (n = 3), *P < 0.05, **P < 0.01, ***P < 0.001, ****P < 0.0001.

zeta potential of PTX/IR780-NMs is ascribed to the encapsulation of positively charged IR780. Since the neutrally charged (zeta potential between –10 and +10 mV) nanomaterials often display higher tumor penetration capacity, PTX/IR780-NMs are considered suitable for application in cancer therapy. The amphiphilic Soluplus® could self-assemble into micelles in an aqueous environment and incorporate water-insoluble PTX and IR780 into the hydrophobic core. The EE of PTX and IR780 was 98.02±1.28% and 90.89±4.96%, respectively (Fig. 2(e)). The stability of PTX/IR780-NMs was investigated at 4 °C for 10 days. As shown in Fig. S1 in the Electronic Supplementary Material (ESM), the particle size of PTX/IR780-NMs remained consistent, indicating the excellent stability of drug-loaded nanomicelles.

Moreover, the fluorescence spectra of IR780 were detected. PTX/IR780-NMs presented a prominent absorption peak at 764 nm in excitation spectrum and 809 nm in emission spectrum consistent with free IR780, suggesting that the encapsulation process resulted in no significant fluorescence property alteration of IR780 (Figs. 2(f) and 2(g)). To determine the influence of laser irradiation on the drug release, we measured the PTX release profiles of PTX/IR780-NMs after being exposed to 808 nm NIR light for 5 min. The micelle samples without laser exposure were set as control. The release profile showed a time-dependent PTX release, and the cumulative release rate reached 50% after 48 h in both groups (Fig. S2 in the ESM). Compared to the control group, the PTX release rate of the laser-treated group was slightly accelerated within the first 12 h (Fig. 2(h)), while the final drug release amount had no statistically significant difference (Fig. S2 in the ESM).

3.2 The photothermal property of PTX/IR780-NMs

IR780 is a prototypic NIR heptamethine cyanine dye with great

photostability and high fluorescence intensity. Upon interaction with NIR light, IR780 can produce an efficient temperature increase. To assess the photothermal property of IR780, PTX/IR780-NMs solution was diluted into different concentrations and treated with laser irradiation (808 nm, 1 W/cm²) for 5 min. Figure 2(i) presented the temperature changes of different samples. The temperature of the pure medium increased slightly along the exposure time, indicating that the medium had no significant effect on the photothermal performance of IR780. By contrast, a noticeable concentration-dependent temperature increase appeared in the groups containing PTX/IR780-NMs. At a low IR780 concentration (2.88 μg/mL), the solution temperature increased by almost 14.3 °C, as the IR780 concentration increased to 4.375 μg/mL, the temperature rapidly raised to 51.2 °C under laser irradiation within 3 min. These results demonstrated that PTX/IR780-NMs had powerful photothermal conversion ability for promising PTT against cancer. To visualize the temperature changes of PTX/IR780-NMs solution, the images were captured every 30 s for 5 min recorded using an infrared thermal imaging camera (Fig. 2(j)). For PTX/IR780-NMs (IR780 concentration: 8.750 μg/mL), the pseudo-color signals gradually deepened with increasing irradiation time, while the pure medium remained nearly unchanged. This result was coincident to the temperature change curves, further confirming that PTX/IR780-NMs had excellent photothermal property.

3.3 *In vitro* cellular uptake and organelle co-localization

To demonstrate the cellular uptake efficiency of PTX/IR780-NMs, C6 was used as a fluorescent probe. As shown in Fig. S3(a) in the ESM, after co-incubation for 0.5 h, the green-fluorescent signal of
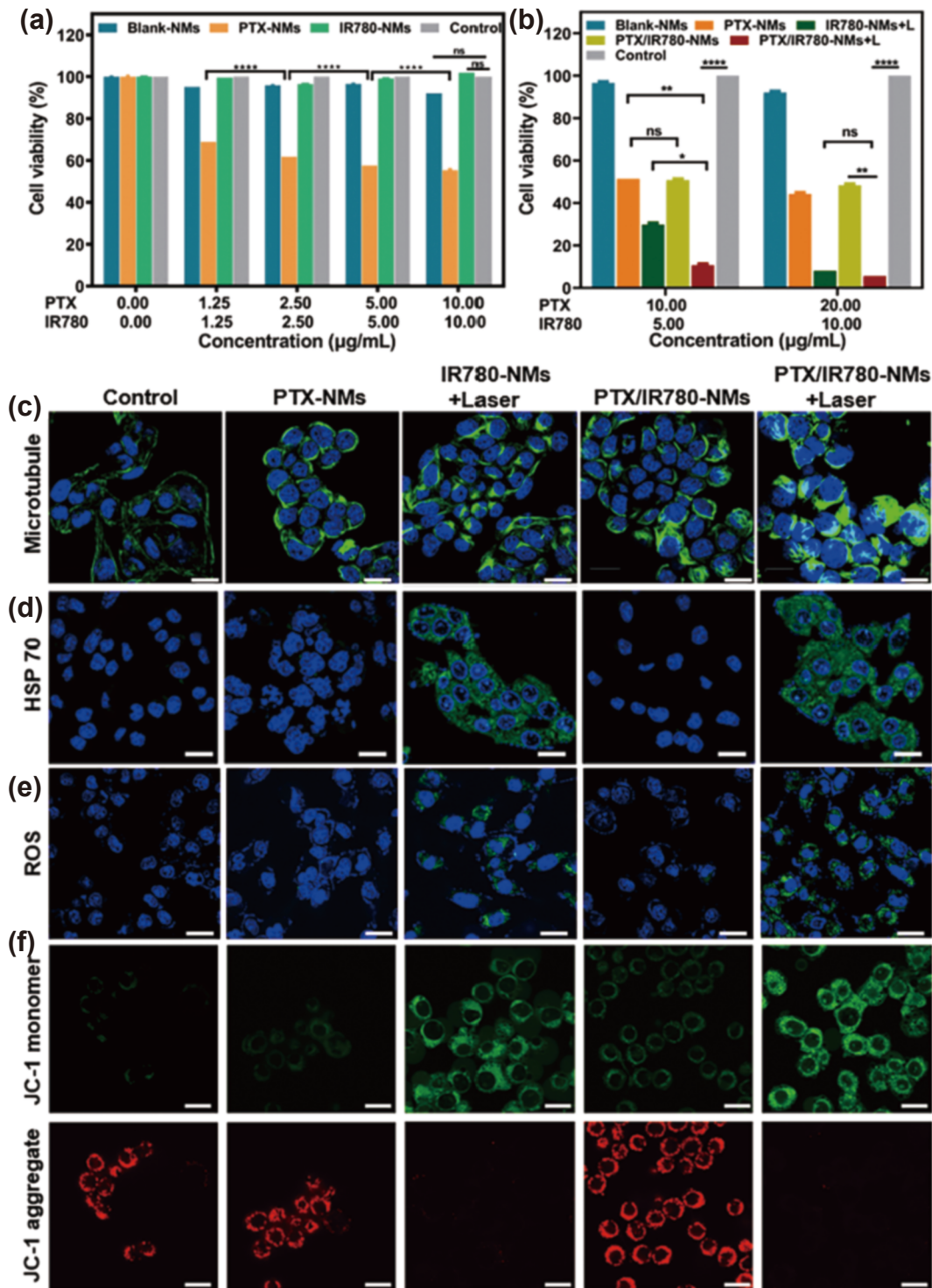
Figure 3 Cell cytotoxicity mechanism of PTX/IR780-NMs. (a) Cell viabilities of B16 cells after incubation with blank NMs, PTX-NMs, and IR780-NMs at different concentrations for 24 h. (b) Cell viabilities of B16 cells after different treatments. CLSM images of (c) microtubule, (d) HSP 70 expression, (e) ROS generation, and (f) JC-1 staining of B16 cells after various treatments. Cell nuclei were stained with DAPI (blue), microtubule, HSP 70, and ROS presented green fluorescence. Scale bar = 20 μm. Data are expressed as mean ± SD ($n = 3$), *$P < 0.05$, **$P < 0.01$, ***$P < 0.001$, ****$P < 0.0001$.

C6 and red-fluorescent signal of IR780 were detected in the cytoplasm, suggesting that the micelles could be rapidly uptaken by B16 cells.

As the incubation time prolonged to 2 h, the cellular uptake of C6/IR780-NMs exhibited a time-dependent increase manner, evidenced by progressively stronger fluorescent signals (Figs. S3(b) and S3(c) in the ESM). Furthermore, the intracellular distribution of C6/IR780-NMs in B16 cells was observed using a CLSM. Commercial mitochondrion-staining agent MitoTracker® Red CMXRos and lysosome-staining agent BBcellProbeTM L03 were

utilized to stain the cells, respectively. Figures S4(a) and S4(b) in the ESM showed that the fluorescent signal of C6/IR780-NMs merged well with the red signal of MitoTracker, and highly overlapped with the signal of the lysosome-staining agent as well. These results confirmed that PTX/IR780-NMs had an excellent organelle-targeting capability, which is beneficial for PTX and IR780 to kill the tumor cells.

3.4 *In vitro* cytotoxicity

Encouraged by the photothermal conversion performance and

efficient cellular uptake, the cytotoxicity of PTX/IR780-NMs in B16 cells was further measured to verify its chemo-photothermal therapeutic effect. The cell viability was quantified by the CCK-8 assay. As shown in Fig. 3(a), cells treated with blank NMs had high cell viability over 92% after 24 h incubation, indicating the good biocompatibility of the nanomicelles. The cell viability of B16 cells with laser treatment was comparable to the control, which implied that laser irradiation had no significant influence on cell proliferation (Fig. S5 in the ESM). For the PTX-NMs group, the cell viability was slightly decreased from 68.86% to 55.38% (PTX concentration: 1.25 and 10.00 μg/mL). For IR780-NMs group, upon laser irradiation, the cell viability presented a remarkable dose-dependent decrease when the IR780 concentration was higher than 1.00 μg/mL (Fig. S6 in the ESM). However, the cell viability showed hardly decline in the absence of laser irradiation (Fig. 3(a)). These results demonstrated that IR780 had no significant dark cytotoxicity, and cell death was mainly ascribed to the IR780-mediated photothermal effect. As shown in Fig. 3(b), a remarkable decrease in cell viability was observed in the combination therapy group compared to the monotherapy groups. The cell viabilities of PTX/IR780-NMs +Laser ("+Laser" means treated with laser irradiation), IR780-NMs +Laser, and PTX-NMs (IR780: 5.00 μg/mL; PTX: 10.00 μg/mL) were 10.74%, 29.93%, and 55.38%, respectively. The above results proved that the combination of chemotherapy and PTT therapy had better tumor cell killing ability than the single therapy, which might because that PTT could increase cell membrane permeation therefore enhancing the chemotherapy sensitivity. Additionally, the further increase in the drug concentration did not cause notably declined cell viability. This might be explained that the high concentration IR780 could generate sufficient hyperpyrexia to kill the cancer cells entirely.

Furthermore, the Calcein-AM/PI co-staining method was used to verify the therapeutic effect. The green fluorescence from Calcein-AM is usually regarded as a signal of living cells, while the red fluorescence from PI represents dead cells. As shown in Fig. S7 in the ESM, PTX/IR780-NMs treated cells plus laser irradiation exhibited stronger red fluorescence than other groups, confirming that PTX/IR780-NMs had superior antitumor capacity due to the chemo-photothermal synergistic therapy.

3.5   Mechanism of chemo-photothermal therapy

To reveal the underlying mechanism of chemo-photothermal therapy, a series of related experiments were conducted. Firstly, the expression of tubulin after different treatments was characterized by immunofluorescent-staining. PTX is a broad-spectrum antitumor drug that promotes tubulin polymerization and inhibits microtubule depolymerization to induce cell apoptosis [27]. Cells treated with PTX had a stronger fluorescent signal of β-tubulin than the control, indicating that nanomicelles could efficiently deliver PTX into the cells to disturb the microtubule dynamics (Fig. 3(c)). In the PTX/IR780-NMs +Laser group, the microtubule of B16 cells were dense aggregates, which was quite different from the filament structure in other groups, suggesting more tubulin polymerization occurred after laser irradiation. This result might be ascribed that PTT-induced hyperthermia increased the cell membrane permeability, then accelerated the cell uptake of micelles, and ultimately increased the intracellular PTX concentration.

Previous experiments showed that PTX/IR780-NMs plus laser irradiation had a remarkable cell-killing effect on B16 cells via chemo-photothermal combination. To reveal the mechanism of PTT-mediated cell damage, the expression level of HSP 70 in B16 cells after laser irradiation was analyzed, which is considered related to increased temperature in the cells [35]. As shown in

Fig. 3(d), a strong fluorescent signal of HSP 70 was observed after treated with IR780-NMs and PTX/IR780-NMs plus laser irradiation, while no apparent fluorescent signal was detected in other groups. This upregulated expression of HSP 70 indicated that IR780 could induce temperature increase upon NIR irradiation, further inducing cell death.

As reported previously, IR780 has a highly efficient quantum yield of singlet oxygen production for potential PDT [36, 37]. The ROS generation in B16 cells after laser irradiation was detected using the DCFH-DA probe. Upon NIR irradiation, the cells treated with IR780-NMs and PTX/IR780-NMs displayed obvious fluorescent signal of ROS, while no visible fluorescent signal was found in other groups (Fig. 3(e)). Since ROS generation principally occurred in mitochondria, the high ROS level may cause mitochondria dysfunction, inducing mitochondria-mediated apoptosis pathway [38, 39]. The mitochondria membrane potential (MMP) disorder is a typical characteristic of mitochondria damage [40]. Thus, changes in the MMP after different treatments was examined using JC-1 probe. As shown in Fig. 3(f), cells treated without laser irradiation exhibited distinct red fluorescence signal (active mitochondria). By contrast, treatment with IR780-NMs and PTX/IR780-NMs plus NIR irradiation resulted in a strong green fluorescence in B16 cells, indicating that MMP was significantly altered after NIR irradiation. These results confirmed that IR780 could induce temperature increase and ROS generation in tumor cells, further resulting in mitochondria dysfunction-mediated irreversible cell damage.

3.6   Fabrication and characterization of PTX/IR780-NMs @DMNs

The nanomicelle-encapsulated DMNs were fabricated by a multistep centrifugation molding technology previously reported (Fig. 4(a)) [41]. The amount of PTX and IR780 loaded in each microneedle patch was 21.69±2.80 μg and 3.07±0.21 μg, respectively. The morphology of PTX/IR780-NMs @DMNs was observed by a camera (Figs. 4(c) and 4(d)) and SEM (Figs. 4(e) and 4(f)). The needles are shaped as a quadrangular pyramid with a height of 800 μm and a base width of 300 μm, which are uniformly arranged into a 12 × 12 array with a 750 μm of tip-to-tip distance. Figure 4(g) showed the residual microneedle base after insertion into the excised rat skin, indicating the good dissolution ability of the DMNs. To visualize the drug distribution in the DMNs, C6/IR780-NMs replaced the PTX/IR780-NMs were encapsulated into the DMNs. As shown in Fig. 4(i), a concentrated distribution of C6 (green fluorescent dots) and IR780 (red fluorescent dots) at the needle tip was observed by CLSM imaging. The 3D reconstruction and layer-by-layer scanning of PTX/IR780-NMs @DMNs were also conducted, and the images were captured by CLSM (Figs. 4(j) and 4(k)).

Furthermore, to verify the self-assembly capacity of the nanomicelle-encapsulated DMNs, the needles were carefully separated from the supporting base and dissolved in the solution (pure water and PBS). The particle size and morphology were measured after complete dissolution of the needles. As shown in Fig. 4(l), the average particle size of samples reconstituted in water and PBS were 64.69 ± 0.32 nm and 66.40 ± 0.36 nm, which was highly coincident to the as-prepared PTX/IR780-NMs. Furthermore, the TEM image displayed the intact sphere structure, which was similar to the morphology of PTX/IR780-NMs showed in Fig. 2(b) (Fig. 4(m)). These results certified that the drug-loaded nanomicelles could be successfully encapsulated into DMNs and spontaneously re-assembled as the DMNs dissolving. It is found that the self-assembled nanomicelles were slightly larger, which might be attributed to the surface coating of
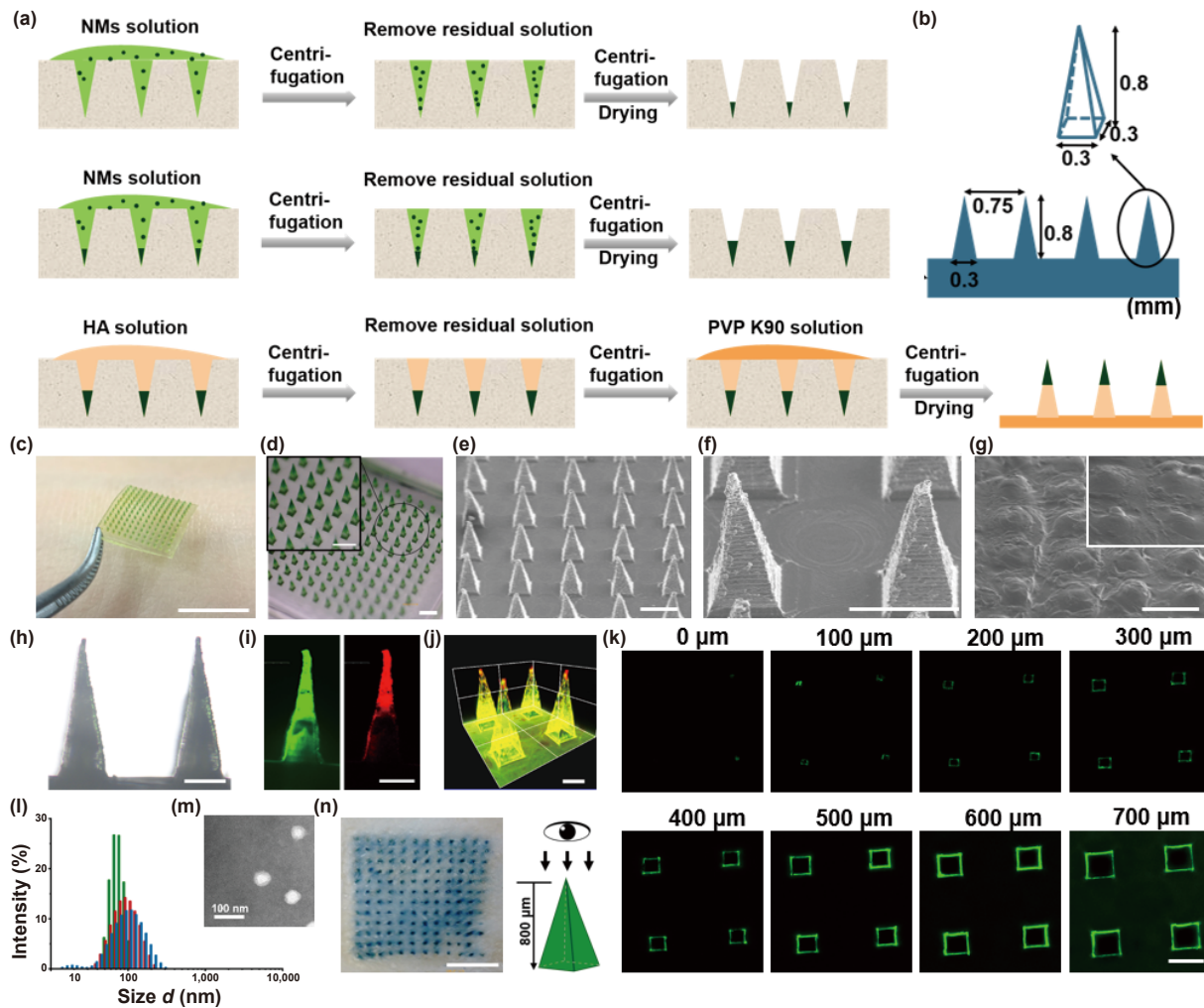
Figure 4 Characterization of PTX/IR780-NMs @DMNs. Schematic illustration of (a) DMN preparation process and (b) DMN structure. (c) and (d) Photographs of PTX/IR780-NMs @DMNs. (c): Scale bar = 1 cm, (d): Scale bar = 1 mm. (e) and (f) SEM images of PTX/IR780-NMs @DMNs. Scale bar = 500 μm. (g) Morphology change of PTX/IR780-NMs @DMNs after dissolution. Scale bar = 500 μm. (h) Microstructure of PTX/IR780-NMs @DMNs. Scale bar = 200 μm. (i) and (j) CLSM images of fluorescent DMNs (green: C6, red: IR780). Scale bar = 200 μm. (k) CLSM images of fluorescent DMNs along *z* axis from tip to base. Scale bar = 300 μm. (l) Particle size of PTX/IR780-NMs (green) and PTX/IR780-NMs @DMNs reconstituted in water (red) and PBS (blue). (m) Morphology of self-assembly PTX/IR780-NMs from DMNs after dissolution. Scale bar = 100 nm. (n) Image of the excised rat dorsal skin after trypan blue @DMNs insertion. Scale bar = 5 mm.

HA during the dissolution process.

Successful skin penetration is the prerequisite for efficient TDD. To assess the skin insertion ability of the DMNs, trypan blue @DMNs were prepared and vertically inserted into the excised rat skin. As shown in Fig. 4(n), a clearly visible blue-spot array corresponding to the DMN puncture sites was presented on the treated skin, demonstrating that the obtained DMNs had enough mechanical strength to pierce the skin for promising percutaneous drug delivery.

3.7 *In vitro* distribution dynamics of PTX/IR780-NMs @DMNs

The *in vitro* drug permeation and distribution after microneedle administration were examined using the fluorescent DMNs and visualized by CLSM. Figure 5(a) were images of the frozen porcine skin sections with fluorescent DMNs insertion for 3, 10, and 30 min. Obvious pore channels were created on the porcine skin surface after microneedle application. And an incompletely dissolved needle was unexpectedly found inside the skin tissue, which further confirmed the successful insertion of the DMNs. Additionally, the fluorescent signal initially distributed around the insertion site and then gradually diffused vertically in the skin as the DMN insertion time prolonged. Further, the horizontal distribution dynamics of drug-loaded nanomicelles were

conducted in the rat skin, which was treated with a fluorescent microneedle and then detected by Z-axis scanning using CLSM for 10 min (Fig. 5(b)). These results verified that PTX/IR780-NMs @DMNs could efficiently penetrate the skin and rapidly dissolved to release drug-loaded nanomicelles, which was beneficial for superior therapeutic efficacy.

3.8 *In vivo* imaging and biodistribution

To investigate the topical drug accumulation and *in vivo* biodistribution, B16 melanoma-bearing mice after administration were monitored using a live fluorescence imaging system. The real-time fluorescence signal of IR780 was recorded at various time points. After PTX/IR780-NMs @DMNs administration, the strongest fluorescent signal at the tumor site appeared at the beginning and gradually decreased (Fig. 5(c) and Fig. S8 in the ESM). For PTX/IR780-NMs I.V. group, the fluorescent signal at the tumor site increased gradually and reached the strongest at 4 h post-administration (Fig. 5(d) and Fig. S8 in the ESM). To further study the biodistribution of drug-loaded nanomicelles, the major organs (heart, liver, spleen, lung, and kidney) were collected 48 h post-administration. As shown in Fig. 5(e), a strong fluorescent signal was observed in the tumor, and little fluorescence signal was found in other organs in the DMNs group. In contrast, the I.V. group showed extensive fluorescence signal in all organs and
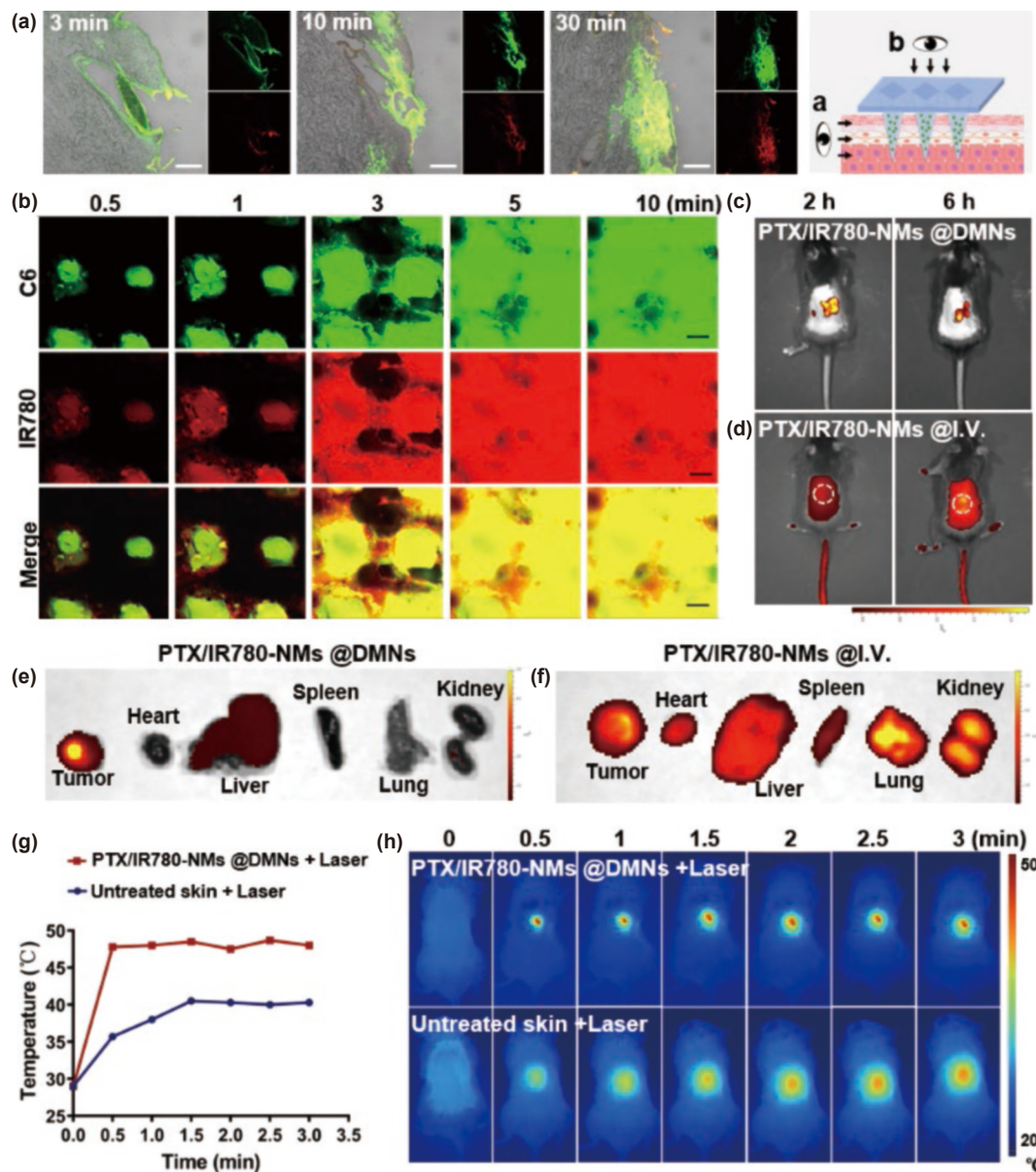
Figure 5 *In vitro* and *in vivo* distribution dynamics of PTX/IR780-NMs @DMNs. Fluorescent images of C6 (green fluorescence) and IR780 (red fluorescence) distribution in the (a) excised porcine skin (cross section) and (b) rat skin (vertical section) after C6/IR780-NMs @DMNs insertion for different time intervals. Scale bar = 200 μm. Fluorescent images of B16 tumor-bearing mice after PTX/IR780-NMs administration by (c) DMN and (d) I.V. Fluorescent images of major organs 48 h post (e) PTX/IR780-NMs @DMNs administration and (f) I.V. (g) Temperature-time profile and (h) photographs of mice under NIR irradiation after PTX/IR780-NMs @DMNs treatment.

mainly accumulated at the liver (Fig. 5(f)). These results confirmed that DMN-based drug delivery could act as a promising strategy to increase tumor accumulation and avoid systemic drug exposure, therefore leading to superior antitumor therapeutic efficacy with reduced side effects.

3.9 *In vivo* photothermal property of PTX/IR780-NMs @DMNs

Encouraged by the excellent photothermal property of PTX/IR780-NMs *in vitro* and the efficient TDD via the DMNs, the photothermal conversion ability of PTX/IR780-NMs @DMNs was investigated *in vivo*. The temperature change in the hair-removed mice's dorsal skin was recorded using an infrared thermal imaging camera. As shown in Figs. 5(g) and 5(h), under laser irradiation for 3 min, the temperature of the untreated bare skin slowly increased from 28 °C to 40 °C. By contrast, the temperature of the mouse skin treated with DMNs plus laser irradiation quickly reached 48 °C within 30 s and remained at such temperature over 2 min, which was high enough to damage the tumor tissues

irreversibly as proved before [42]. These results indicated that the obtained PTX/IR780-NMs @DMNs was promising to achieve efficient PTT antitumor treatment.

3.10 *In vivo* antitumor efficacy

Finally, the *in vivo* antitumor efficacy of PTX/IR780-NMs@DMNs was conducted in the subcutaneous B16 melanoma-bearing C57 mice model. Figure 6(a) is the schematic diagram of the therapeutic schedule. Tumor-bearing mice were randomly divided into 5 groups and administrated with different treatments. As shown in Fig. 6(b), the tumor volume of mice in the control group exhibited exponential growth and quickly reached 2,000 mm³, indicating the malignant proliferation of melanoma. The group with PTX-NMs @DMNs treatment showed a modest inhibition of tumor growth, which was similar to the mice receiving PTX/IR780-NMs @DMNs treatment without laser irradiation. In the presence of laser treatment, the PTX/IR780-NMs @DMNs group exhibited a remarkable tumor growth inhibition compared to other groups (Fig. 6(e)). Furthermore, after a course of study, the mice were
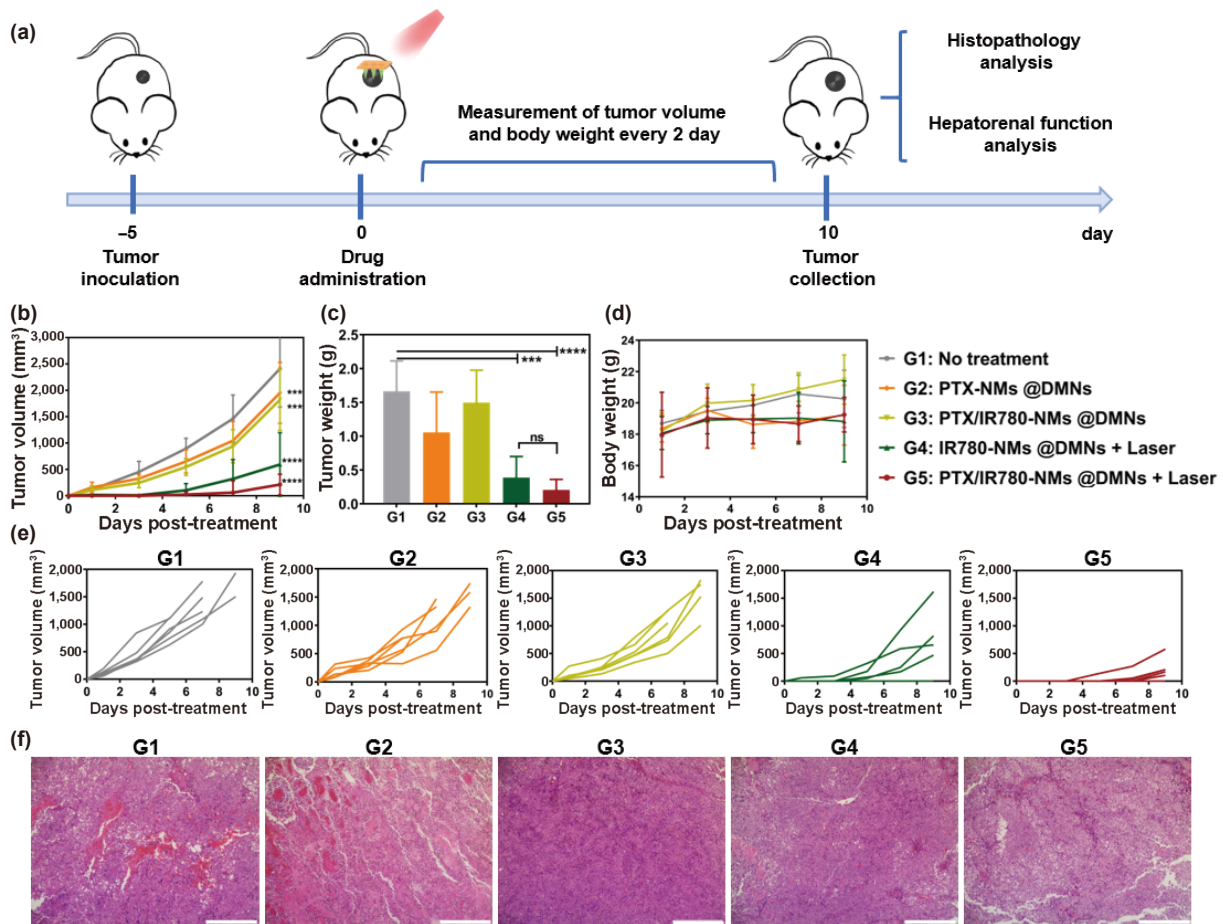
Figure 6 *In vivo* antitumor experiment. (a) Schematic diagram of the therapeutic model. (b) Tumor volume, (c) tumor weight, and (d) body weight of mice after various treatments. (e) Tumor growth curve of each mice after various treatments (*n* = 6). (f) H&E staining of tumors after various treatments. Scale bar = 400 μm. Data are expressed as the mean ± SD (*n* = 6), *$P < 0.05$, **$P < 0.01$, ***$P < 0.001$, ****$P < 0.0001$.

sacrificed and the tumors were resected and weighed. The result of the tumor weight was consistent with the tumor growth curve (Fig. 6(c)). In the control group, the tumor size enlarged over the whole experiment and reached the largest tumor weight, while the PTX/IR780-NMs @DMNs +Laser group had the smallest tumor volume than other groups. The tumor growth inhibitory rates of PTX-NMs @DMNs, IR780-NMs @DMNs +Laser, and PTX/IR780-NMs @DMNs +Laser were 36.5%, 76.7%, and 87.7%, respectively (Fig. S9 in the ESM). These results indicated that the combination of chemo-photothermal therapy had superior tumor inhibition efficacy than monotherapy. Moreover, the H&E staining sections of tumor tissue were observed to further verify the antitumor effect. H&E staining results showed apparent cell shrinkage and nuclei absence in the PTX/IR780-NMs @DMNs +Laser group, which also confirmed the severe cell damage and inhibited tumor growth (Fig. 6(f)). These results confirmed that chemo-photothermal therapy could synergistically improve the antitumor efficacy.

3.11 Safety evaluation

To investigate the biocompatibility, the PTX/IR780-NMs @DMNs was applied on the dorsal skin of mice to observe the skin recovery after DMN insertion (Fig. S10 in the ESM). The treated skin showed clear puncture spots at the DMN insertion site, which gradually recovered within 3 days without leaving any scar. When cooperatively treated with irradiation, slight redness and swelling appeared in the DMNs pierced skin, but they gradually subsided within 10 days, suggesting the great safety of PTX/IR780-NMs @DMNs plus irradiation. As shown in Fig. 6(d), the body weight of mice did not change except for the control group due to the

rapid tumor growth. The major organs were collected for the histopathology study (Fig. 7(a)). No evident inflammatory or damage was found in all DMNs treated groups, which further suggested that DMN treatment did not induce any significant side effects or toxicities. Additionally, the blood samples from mice were function. As shown in Fig. 7(b), the PTX/IR780-NMs @DMNs treated mice displayed no abnormality compared to the standard of healthy mice, indicating this treatment had no impact on the also collected for evaluating liver and kidney function. ALT (alanine aminotransferase) and AST (aspartate aminotransferase) were two indicators for liver function, and UREA (urea nitrogen) and CREA (creatinine) were makers for kidney physiological function of the liver and kidney. Collectively, these results indicated that PTX/IR780-NMs @DMNs had both outstanding anticancer efficacy and reliable safety for cancer therapy.

4 Conclusions

In summary, a self-assembly Nano-DMN drug delivery system was successfully constructed for chemo-photothermal combination therapy against melanoma. The *in vivo* experiments showed that the PTX/IR780-NMs @DMNs significantly inhibited tumor growth without any side effects in a melanoma mice model. This result mainly attributed to the "nano in micro" strategy, which could directly "shoot" at the tumor site to achieve maximized tumor accumulation, subsequently *in situ* self-assembly into cargo-encapsulated nanomicelles along with the dissolution of DMNs, ultimately promote the permeation into deep tumor tissues. This work demonstrated that such a strategy could serve as a potential local co-delivery platform to achieve synergistic therapeutic efficacy in superficial diseases.
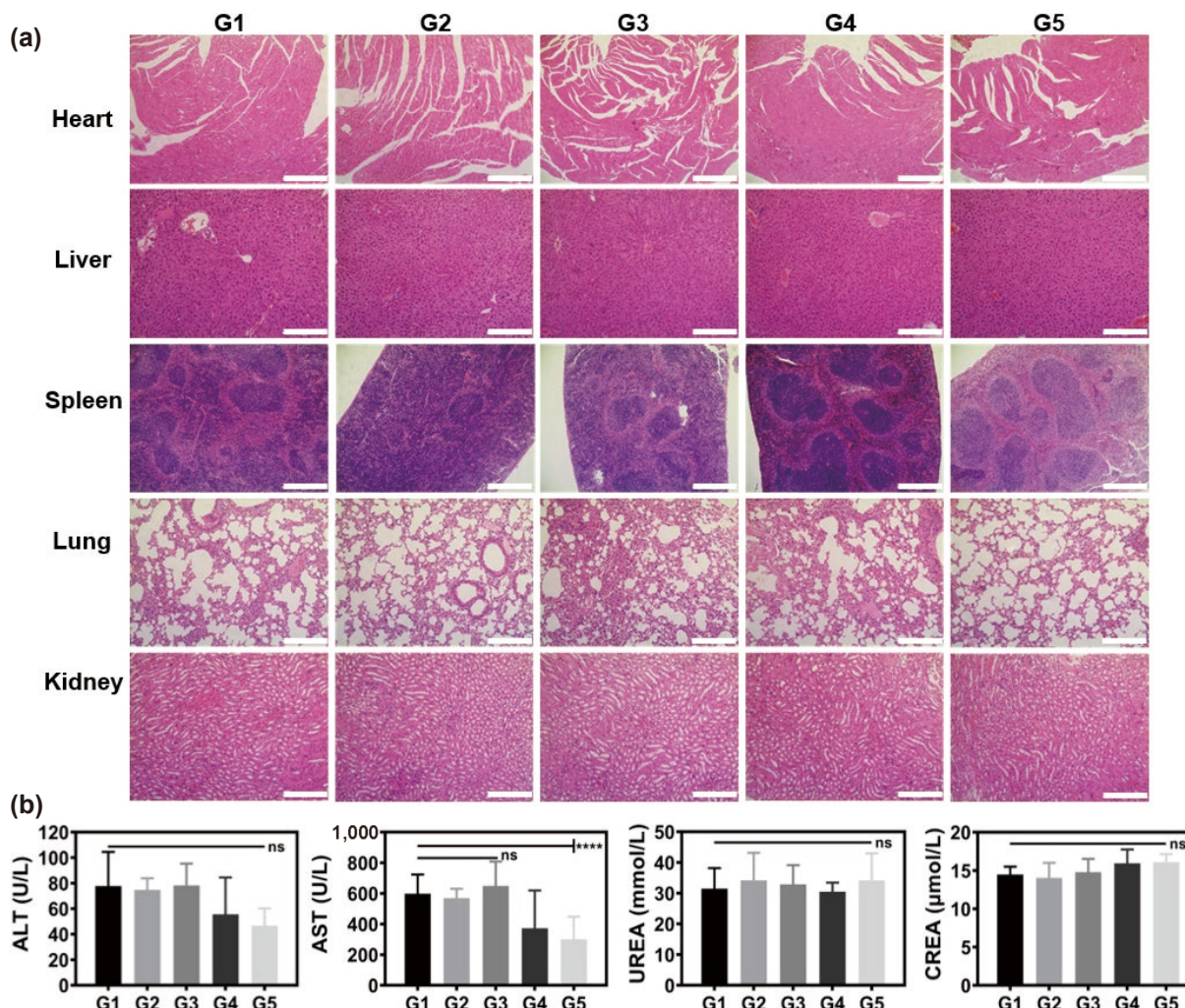
Figure 7 Safety evaluation of PTX/IR780-NMs @DMNs. (a) H&E staining of major organs from mice after different treatments. Scale bar = 400 μm. (b) Liver and kidney function examination parameters of mice after different treatments (mean ± SD, *n* = 3). G1: No treatment, G2: PTX-NMs @DMNs, G3: PTX/IR780-NMs @DMNs, G4: IR780-NMs @DMNs +Laser, G5: PTX/IR780-NMs @DMNs +Laser.

Acknowledgements

Electronic Supplementary Material: Supplementary material (materials; particle size stability of PTX/IR780-NMs; drug release profile of PTX from PTX/IR780-NMs; CLSM images of cellular uptake and organelle colocalization of PTX/IR780-NMs in B16 cells; cell viability of B16 cells after different treatments; fluorescent images of tumor-bearing mice after PTX/IR780-NMs administration by DMN and I.V.; tumor inhibition rate after various treatments; skin recovery of mice after DMN administration) is available in the online version of this article at https://doi.org/10.1007/s12274-021-3817-x.

References

[1] Pires, L. R.; Gaspar, J. Micro and nano-needles as innovative approach in nanomedicine. In *Nanostructured Biomaterials for Regenerative Medicine*. Guarino, V; Iafisco, M; Spriano, S., Eds.; Woodhead Publishing Ltd: Oxford, 2020; pp 379–406.

[2] Yuan, A.; Qiu, X. F.; Tang, X. L.; Liu, W.; Wu, J. H.; Hu, Y. Q. Self-assembled PEG-IR-780-C13 micelle as a targeting, safe and highly-effective photothermal agent for *in vivo* imaging and cancer therapy. *Biomaterials* **2015**, *51*, 184–193.

[3] Shu, M.; Tang, J. J.; Chen, L. L.; Zeng, Q.; Li, C.; Xiao, S. T.; Jiang, Z. Z.; Liu, J. Tumor microenvironment triple-responsive nanoparticles enable enhanced tumor penetration and synergetic chemo-photodynamic therapy. *Biomaterials* **2020**, *268*, 120574.

[4] Zhang, Y. R.; Lin, R.; Li, H. J.; He, W. L.; Du, J. Z.; Wang, J. Strategies to improve tumor penetration of nanomedicines through nanoparticle design. *Wiley Interdiscip. Rev. Nanomed. Nanobiotechnol.* **2019**, *11*, e1519.

[5] Cong, Z. Q.; Zhang, L.; Ma, S. Q.; Lam, K. S.; Yang, F. F.; Liao, Y. H. Size-transformable hyaluronan stacked self-assembling peptide nanoparticles for improved transcellular tumor penetration and photo-chemo combination therapy. *ACS Nano* **2020**, *14*, 1958–1970.

[6] Cong, Z. Q.; Yang, F. F.; Cao, L.; Wen, H.; Fu, T. T.; Ma, S. Q.; Liu, C. Y.; Quan, L. H.; Liao, Y. H. Multispectral optoacoustic tomography (MSOT) for imaging the particle size-dependent intratumoral distribution of polymeric micelles. *Int. J. Nanomedicine* **2018**, *13*, 8549–8560.

[7] Chen, H. M.; Zhang, W. Z.; Zhu, G. Z.; Xie, J.; Chen, X. Y. Rethinking cancer nanotheranostics. *Nat. Rev. Mater.* **2017**, *2*, 17024.

[8] Jiang, T. Y.; Wang, T.; Li, T.; Ma, Y. D.; Shen, S. Y.; He, B. F.; Mo, R. Enhanced transdermal drug delivery by transfersome-embedded oligopeptide hydrogel for topical chemotherapy of melanoma. *ACS Nano* **2018**, *12*, 9693–9701.

[9] Kim, N. W.; Kim, S. Y.; Lee, J. E.; Yin, Y.; Lee, J. H.; Lim, S. Y.; Kim, E. S.; Duong, H. T. T.; Kim, H. K.; Kim, S. et al. Enhanced cancer vaccination by *in situ* nanomicelle-generating dissolving microneedles. *ACS Nano* **2018**, *12*, 9702–9713.

[10] Pei, P.; Yang, F.; Liu, J. X.; Hu, H. R.; Du, X. Y.; Hanagata, N.;

Zhao, S. C.; Zhu, Y. F. Composite-dissolving microneedle patches for chemotherapy and photothermal therapy in superficial tumor treatment. *Biomater. Sci.* **2018**, *6*, 1414–1423.

[11] Boopathy, A. V.; Mandal, A.; Kulp, D. W.; Menis, S.; Bennett, N. R.; Watkins, H. C.; Wang, W. D.; Martin, J. T.; Thai, N. T.; He, Y. P. et al. Enhancing humoral immunity via sustained-release implantable microneedle patch vaccination. *Proc. Natl. Acad. Sci. USA* **2019**, *116*, 16473–16478.

[12] Waghule, T.; Singhvi, G.; Dubey, S. K.; Pandey, M. M.; Gupta, G.; Singh, M.; Dua, K. Microneedles: A smart approach and increasing potential for transdermal drug delivery system. *Biomed. Pharmacother.* **2019**, *109*, 1249–1258.

[13] Li, W. T.; Peng, J. R.; Yang, Q.; Chen, L. J.; Zhang, L.; Chen, X. X.; Qian, Z. Y. α-Lipoic acid stabilized DTX/IR780 micelles for photoacoustic/fluorescence imaging guided photothermal therapy/chemotherapy of breast cancer. *Biomater. Sci.* **2018**, *6*, 1201–1216.

[14] Deng, Y. Y.; Käfer, F.; Chen, T. T.; Jin, Q.; Ji, J.; Agarwal, S. Let there be light: Polymeric micelles with upper critical solution temperature as light-triggered heat nanogenerators for combating drug-resistant cancer. *Small* **2018**, *14*, 1802420.

[15] DeMuth, P. C.; Min, Y.; Irvine, D. J.; Hammond, P. T. Implantable silk composite microneedles for programmable vaccine release kinetics and enhanced immunogenicity in transcutaneous immunization. *Adv. Healthc. Mater.* **2014**, *3*, 47–58.

[16] DeMuth, P. C.; Moon, J. J.; Suh, H.; Hammond, P. T.; Irvine, D. J. Releasable layer-by-layer assembly of stabilized lipid nanocapsules on microneedles for enhanced transcutaneous vaccine delivery. *ACS Nano* **2012**, *6*, 8041–8051.

[17] Chen, C. H.; Shyu, V. B. H.; Chen, C. T. Dissolving microneedle patches for transdermal insulin delivery in diabetic mice: Potential for clinical applications. *Materials (Basel)* **2018**, *611*, 1625.

[18] Chen, G. J.; Yu, J. C.; Gu, Z. Glucose-responsive microneedle patches for diabetes treatment. *J. Diabetes Sci. Technol.* **2019**, *13*, 41–48.

[19] Lee, I. C.; Lin, W. M.; Shu, J. C.; Tsai, S. W.; Chen, C. H.; Tsai, M. T. Formulation of two-layer dissolving polymeric microneedle patches for insulin transdermal delivery in diabetic mice. *J. Biomed. Mater. Res. Part A* **2017**, *105*, 84–93.

[20] Tham, H. P.; Xu, K. M.; Lim, W. Q.; Chen, H. Z.; Zheng, M. J.; Thng, T. G. S.; Venkatraman, S. S.; Xu, C. J.; Zhao, Y. L. Microneedle-assisted topical delivery of photodynamically active mesoporous formulation for combination therapy of deep-seated melanoma. *ACS Nano* **2018**, *12*, 11936–11948.

[21] Yang, P. P.; Lu, C.; Qin, W. B.; Chen, M. L.; Quan, G. L.; Liu, H.; Wang, L. L.; Bai, X. Q.; Pan, X.; Wu, C. B. Construction of a core-shell microneedle system to achieve targeted co-delivery of checkpoint inhibitors for melanoma immunotherapy. *Acta Biomater.* **2020**, *104*, 147–157.

[22] Wu, B. Y.; Fu, J. T.; Zhou, Y. X.; Luo, S. L.; Zhao, Y. T.; Quan, G. L.; Pan, X.; Wu, C. B. Tailored core-shell dual metal-organic frameworks as a versatile nanomotor for effective synergistic antitumor therapy. *Acta Pharm. Sin. B* **2020**, *10*, 2198–2211.

[23] Wang, B.; Wu, S.; Lin, Z.; Jiang, Y.; Chen, Y.; Chen, Z. S.; Yang, X.; Gao, W. A personalized and long-acting local therapeutic platform combining photothermal therapy and chemotherapy for the treatment of multidrug-resistant colon tumor. *Int. J. Nanomedicine* **2018**, *13*, 8411–8427.

[24] Moreira, A. F.; Rodrigues, C. F.; Jacinto, T. A.; Miguel, S. P.; Costa, E. C.; Correia, I. J. Poly(vinyl alcohol)/chitosan layer-by-layer microneedles for cancer chemo-photothermal therapy. *Int. J. Pharm.* **2020**, *576*, 118907.

[25] Yuan, X.; Yin, Y. L.; Zan, W.; Sun, X. Y.; Yang, Q. Hybrid manganese dioxide-bovine serum albumin nanostructure incorporated with doxorubicin and IR780 for enhanced breast cancer chemo-photothermal therapy. *Drug Deliv.* **2019**, *26*, 1254–1264.

[26] Zhang, L. H.; Qin, Y.; Zhang, Z. M.; Fan, F.; Huang, C. L.; Lu, L.; Wang, H.; Jin, X.; Zhao, H. X.; Kong, D. L. et al. Dual pH/reduction-responsive hybrid polymeric micelles for targeted chemo-photothermal combination therapy. *Acta Biomater.* **2018**, *75*, 371–385.

[27] Qin, W. B.; Quan, G. L.; Sun, Y.; Chen, M. L.; Yang, P. P.; Feng, D. S.; Wen, T.; Hu, X. Y.; Pan, X.; Wu, C. B. Dissolving microneedles with spatiotemporally controlled pulsatile release nanosystem for synergistic chemo-photothermal therapy of melanoma. *Theranostics* **2020**, *10*, 8179–8196.

[28] Zhao, D. J.; Zhang, H. Y.; Yang, S. F.; He, W. X.; Luan, Y. X. Redox-sensitive mPEG-SS-PTX/TPGS mixed micelles: An efficient drug delivery system for overcoming multidrug resistance. *Int. J. Pharm.* **2016**, *515*, 281–292.

[29] Alves, C. G.; Lima-Sousa, R.; de Melo-Diogo, D.; Louro, R. O.; Correia, I. J. IR780 based nanomaterials for cancer imaging and photothermal, photodynamic and combinatorial therapies. *Int. J. Pharm.* **2018**, *542*, 164–175.

[30] Bernabeu, E.; Gonzalez, L.; Cagel, M.; Gergic, E. P.; Moretton, M. A.; Chiappetta, D. A. Novel Soluplus®-TPGS mixed micelles for encapsulation of paclitaxel with enhanced *in vitro* cytotoxicity on breast and ovarian cancer cell lines. *Colloids Surf. B: Biointerfaces* **2016**, *140*, 403–411.

[31] Jin, X.; Zhou, B.; Xue, L. Z.; San, W. G. Soluplus® micelles as a potential drug delivery system for reversal of resistant tumor. *Biomed. Pharmacother.* **2015**, *69*, 388–395.

[32] Pinto, J. M. O.; Rengifo, A. F. C.; Mendes, C.; Leão, A. F.; Parize, A. L.; Stulzer, H. K. Understanding the interaction between Soluplus®and biorelevant media components. *Colloids Surf. B: Biointerfaces* **2020**, *187*, 110673.

[33] Zhu, C. L.; Gong, S.; Ding, J. S.; Yu, M. R.; Ahmad, E.; Feng, Y.; Gan, Y. Supersaturated polymeric micelles for oral silybin delivery: The role of the Soluplus-PVPVA complex. *Acta Pharm. Sin. B* **2019**, *9*, 107–117.

[34] Chen, M. L.; Yang, D.; Sun, Y.; Liu, T.; Wang, W. H.; Fu, J. T.; Wang, Q. Q.; Bai, X. Q.; Quan, G. L.; Pan, X.; Wu, C. B. *In situ* self-assembly nanomicelle microneedles for enhanced photoimmunotherapy via autophagy regulation strategy. *ACS Nano* **2021**, *15*, 3387–3401.

[35] Tang, H. M.; Kobayashi, H.; Niidome, Y.; Mori, T.; Katayama, Y.; Niidome, T. CW/pulsed NIR irradiation of gold nanorods: Effect on transdermal protein delivery mediated by photothermal ablation. *J. Control. Release* **2013**, *171*, 178–183.

[36] Pais-Silva, C.; de Melo-Diogo, D.; Correia, I. J. IR780-loaded TPGS-TOS micelles for breast cancer photodynamic therapy. *Eur. J. Pharm. Biopharm.* **2017**, *113*, 108–117.

[37] Jiang, C. X.; Cheng, H.; Yuan, A. H.; Tang, X. L.; Wu, J. H.; Hu, Y. Q. Hydrophobic IR780 encapsulated in biodegradable human serum albumin nanoparticles for photothermal and photodynamic therapy. *Acta Biomater.* **2015**, *14*, 61–69.

[38] Tan, Y. N.; Zhu, Y.; Wen, L. J.; Yang, X. Q.; Liu, X.; Meng, T. T.; Dai, S. H.; Ping, Y.; Yuan, H.; Hu, F. Q. Mitochondria-responsive drug release along with heat shock mediated by multifunctional glycolipid micelles for precise cancer chemo-phototherapy. *Theranostics* **2019**, *9*, 691–707.

[39] Burke, P. J. Mitochondria, bioenergetics and apoptosis in cancer. *Trends Cancer* **2017**, *3*, 857–870.

[40] Zhang, J. F.; Fang, F.; Liu, B.; Tan, J. H.; Chen, W. C.; Zhu, Z. L.; Yuan, Y.; Wan, Y. P.; Cui, X.; Li, S. L. et al. Intrinsically cancer-mitochondria-targeted thermally activated delayed fluorescence nanoparticles for two-photon-activated fluorescence imaging and photodynamic therapy. *ACS Appl. Mater. Interfaces* **2019**, *11*, 41051–41061.

[41] Lin, S. Q.; Quan, G. L.; Hou, A. L.; Yang, P. P.; Peng, T. T.; Gu, Y. K.; Qin, W. B.; Liu, R. B.; Ma, X. Y.; Pan, X. et al. Strategy for hypertrophic SCAR therapy: Improved delivery of triamcinolone acetonide using mechanically robust tip-concentrated dissolving microneedle array. *J. Control. Release* **2019**, *306*, 69–82.

[42] Coral, D. F.; Soto, P. A.; Blank, V.; Veiga, A.; Spinelli, E.; Gonzalez, S.; Saracco, G. P.; Bab, M. A.; Muraca, D.; Setton-Avruj, P. C. et al. Nanoclusters of crystallographically aligned nanoparticles for magnetic thermotherapy: Aqueous ferrofluid, agarose phantoms and *ex vivo* melanoma tumour assessment. *Nanoscale* **2018**, *10*, 21262–21274.